Stony Brook University

The official electronic file of this thesis or dissertation is maintained by the University Libraries on behalf of The Graduate School at Stony Brook University.

Preparation and Investigation of Multi-alkali Photocathode

A Thesis Presented

by

Xue Liang

to

The Graduate School

in Partial Fulfillment of the

Requirements

for the Degree of

Master of Science

in

Materials Science and Engineering

Stony Brook University

December 2013

Stony Brook University

The Graduate School

Xue Liang

We, the thesis committee for the above candidate for the

Master of Science degree, hereby recommend

acceptance of this thesis.

Ilan Ben-Zvi, Senior Scientist
Division Head, Accelerator R&D Division
Associate Chair, Collider-Accelerator Department
Brookhaven Professor, Physics and Astronomy Department
Stony Brook University

Michael Dudley, Professor
Chair, Materials Science and Engineering Department
Stony Brook University

John Smedley, Physicist
Instrumentation Division
Brookhaven National Laboratory

Erik Muller, Research Assistant Professor
Physics and Astronomy
Adjunct Professor
Materials Science and Engineering
Stony Brook University

This thesis is accepted by the Graduate School

Charles Taber
Dean of the Graduate School

ii

Abstract of the Thesis

Preparation and Investigation of Multi-alkali Photocathode

by

Xue Liang

Master of Science

in

Materials Science and Engineering

Stony Brook University

2013

Multialikali antimonide photocathodes exhibit high quantum efficiency in visible light range, so this kind of cathodes is attractive for use in high average current photoinjectors to generate high quality electron beams. We have grown multi-alkali photocathodes on silicon (100) substrates, simultaneously acquiring in-situ X-ray reflection (XRR), X-ray diffraction (XRD) and X-ray photoelectron spectroscopy (XPS) data throughout the growth process. Correlations between cathode structure and growth parameters and the resulting quantum efficiency (QE) have been explored.

Table of Contents

List of Figures/Tables/Illustrations

List of Abbreviations

ERL: Energy Recovery Linac
FEL: Free Electron Laser
QE: Quantum Efficiency
RF: Radio Frequency
UV: Ultraviolet
PEA: Positive Electron Affinity
NEA: Negative Electron Affinity
BNL: Brookhaven National Lab
RHIC: Relativistic Heavy Ion Collider
SRF: Superconducting Radio Frequency
CAD: Collider Accelerator Department
NSLS: National Synchrotron Light Source
UHV: Ultra High Vacuum
XRR: X-ray Reflectivity
XRD: X-ray Diffraction
FTM: Film Thickness Monitor
XPS: X-ray photoelectron spectroscopy
CHESS: Cornell High Energy Synchrotron Source
GI-SAXS: Grazing Incidence Small Angle X-ray Scatterin

1 Introduction

1.1 The requirement of electron source for ERL based light source

Compared with normal X-ray produced by conventional X-ray tubes, synchrotron radiation facilities have unparalleled capability to produce higher brightness and intensity X-ray beams. The technology of synchrotron light source has already been widely used in so many areas such as materials science, biology, condensed matter physics and medicine.

To meet the growing demand from these science areas, the development of new generation synchrotron radiation sources has begun. At the same time Energy Recovery Linac (ERL) based light source is made possible by fast developing of superconducting accelerators technology and electron sources research. The brightness of synchrotron radiation which ERL generate can be thousands times greater than that of storage rings we used today. [1-4]

The selection of the cathode material and the corresponding laser is dictated by the beam current and emittance requirements of the application. Some free electron laser (FEL) facilities used thermionic cathode such as LaB_6 [33]. This kind of cathodes is very stable against contaminated environment and has uniform emission density. However, it is difficult to get low energy spread beam from a thermionic cathode. As a result, this kind of cathodes cannot meet the requirement of high current ERL.

Metal photocathodes are highly suitable for low repetition rate, high peak brightness injectors. However, the inherent low quantum efficiency (QE) and high requirement on photon energy push an inordinate stress on the laser development. As a result, the focus turns to cathode materials with high QE at longer wavelengths, preferably in the visible range. Semiconductor photocathode such as K_2CsSb and V-III semiconductor can get very high QE. They can easily be excited via visible laser. This kind of photocathode is regarded as the best option for the realization of ERL based new generation light source.

The design of photocathodes for ERL based light source is one of the key challenges for new generation accelerator based light source. Most of both types of sources require high QE at visible laser as well as very low thermal emittance electron beams from the cathode. [5] How to fabricate qualified photocathode is an area requiring significant support.

Alkali antimonide is a prime candidate for next generation photoinjectors. But many materials science problems such as roughness, lifetime, etc need to be explored before they can be adopted as robust technologies and used in a RF gun. [6, 7]

Photoinjectors are required to produce high bright electron beam and low emittance. Hence, the photocathode is expected to deliver high current and optimum emittance. Further, the cathode has to have prompt temporal response. Finally, the cathode should be robust enough to work in the real gun vacuum conditions. And higher power laser in the visible range is easier to build and operate compare to a UV laser with similar power level. Hence the visible light responded photocathode is one of the best candidate cathodes for next generation light source. [7-9]
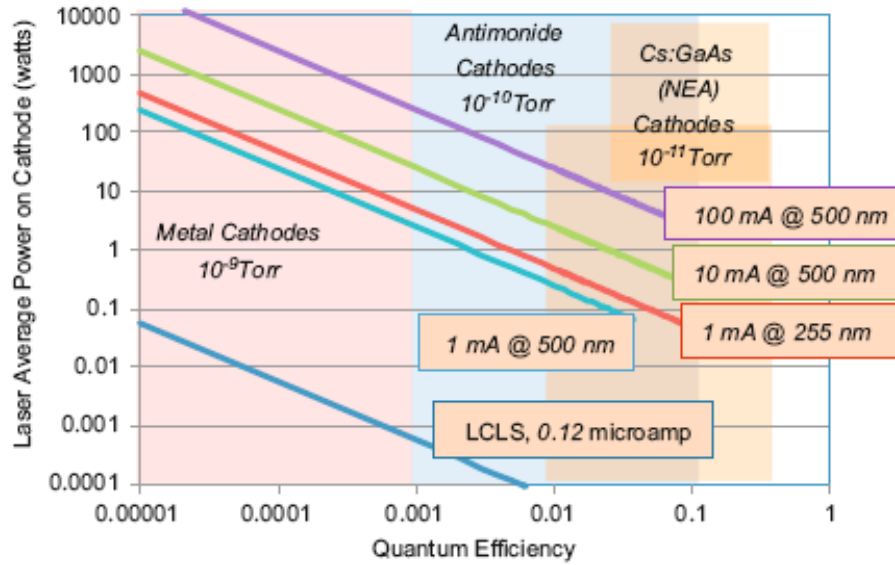
Fig1. Quantum Efficiency of different types of photocathode [3]

Metal photocathodes are very robust, so they do not need high stringent vacuum requirements. But, they can emit only in UV light and have a very low quantum efficiency (QE). Semiconductor cathodes, on the other hand, they are very sensitive to vacuum conditions. Such UHV makes the fabrication and handling is a challengeing.

Cathode Type	Cathode	Typical Wavelength, λ_{opt}(nm), (eV)	Quantum Efficiency (electrons per photon)	Vacuum for 1000 Hrs (Torr)	Gap Energy + Electron Affinity, $E_A + E_G$ (eV)	Thermal Emittance (microns/mm(rms))	
						Eqn. [7]	Expt.
PEA: Mono-alkali	Cs_2Te	211, 5.88	~0.1	10^{-9}	3.5 [42]	1.2	0.5±0.1 [35]
		264, 4.70	-	-	"	0.9	0.7±0.1 [35]
		262, 4.73	-	-	"	0.9	1.2±0.1 [43]
	Cs_3Sb	432, 2.87	0.15	?	1.6 + 0.45 [42]	0.7	?
	K_3Sb	400, 3.10	0.07	?	1.1 + 1.6 [42]	0.5	?
	Na_3Sb	330, 3.76	0.02	?	1.1 + 2.44 [42]	0.4	?
	Li_3Sb	295, 4.20	0.0001	?	?	?	?
PEA: Multi-alkali	Na_2KSb	330, 3.76	0.1	10^{-10}	1+1 [42]	1.1	?
	$(Cs)Na_3KSb$	390, 3.18	0.2	10^{-10}	1+0.55 [42]	1.5	?
	K_2CsSb	543, 2.28	0.1	10^{-10}	1+1.1 [42]	0.4	?
	$K_2CsSb(O)$	543, 2.28	0.1	10^{-10}	1+<1.1 [42]	~0.4	?
NEA	GaAs(Cs,F)	532, 2.33	~0.1	?	1.4±0.1 [42]	0.8	0.44±0.01 [44]
		860, 1.44	-	?	"	0.2	0.22±0.01 [44]
	GaN(Cs)	260, 4.77	-	?	1.96 + ? [44]	1.35	1.35±0.1 [45]
	GaAs(1-x)Px x~0.45 (Cs,F)	532, 2.33	-	?	1.96+? [44]	0.49	0.44±0.1 [44]
S-1	Ag-O-Cs	900, 1.38	0.01	?	0.7 [42]	0.7	?

Fig 2 Properties of the Semiconductor Cathodes [3]

Among the semiconductor cathodes, Positive Electron Affinity (PEA) Multi-Alkali cathodes require more stringent growth environment compared with Negative Electron Affinity (NEA) cathodes, such as GaAs. NEA cathodes usually have higher QE. A PEA cathode such as Multi-alkali is a potential choice for using in photoinjectors.

In the past decade, NEA and PEA semiconductor cathodes such as GaAs:Cs, GaN:Cs, CsTe and multi-alkali cathodes have great development. The research interest is focused on the development of reliable, long-lived photocathodes with fast time response and high levels of reproducibility.[10-12]

The alkali antimonides are a broad class of materials, some of which have extraordinary photo-emissive properties. They can be split into the mono-, bi- and multi-alkali antimonides, with the latter in general having a response further into the infrared part of the spectrum. Of these, the bi–alkalis containing potassium and cesium appear to be some of the most useful in terms of high quantum yield at low photon energy. The development of multi-alkali photocathode started in 1960s, and its preparation and characteristics were investigated by a number of scientists. [13-15] Such cathodes have been used in some DC and normal RF photoinjectors. [16-18]

1.2   The development of multi alkali photocathode

Since A.H. Sommer discovered that two alkali metals such as Na, K, combined with antimonide, have higher sensitivity and wider spectral response [34], the researches of photocathode based on antimonide with the alkali metals have been considered as one of the most important method to get high quantum efficiency (QE) photocathodes. [19-21]

The chemical methods used in the past were not accurate enough to prove or disprove the existence of excess Sb in Cs_3Sb of maximum sensitivity. McCarroll and Simon achieved a further improvement in the determination of cathode structure. [34] They designed an electron diffraction camera that allows not only the examination of the cathode material in-situ, but also could observe of structural changes during cathode formation.

K_2CsSb is low emittance, green light sensitive, and with high QE. This type of cathode has already been used in an RF injector of an FEL for the first time at Boeing- Los Alamos project by D.H. Dowell.[17] Their work was hindered by poor vacuum in the high frequency RF gun, and high partial pressures of water. This material would satisfy most of the requirements for a high current injector. The lifetime of the cathode in these measurement dependents on the partial pressure of water vapor in the vacuum. With the advent of superconducting RF cavities with naturally excellent vacuum characteristics, this material is a possible choice.

1.2.1   Crystal Structure of Multi-alkali photocathode

Kalarasse described the DO_3 cubic structure of K_2CsSb photocathode. [35] As shown in fig 3, the antimony atoms are in the first sublattice. And the second and fourth sublattices are occupied by the first alkali atons. . The M_I occupies the third sublattice.
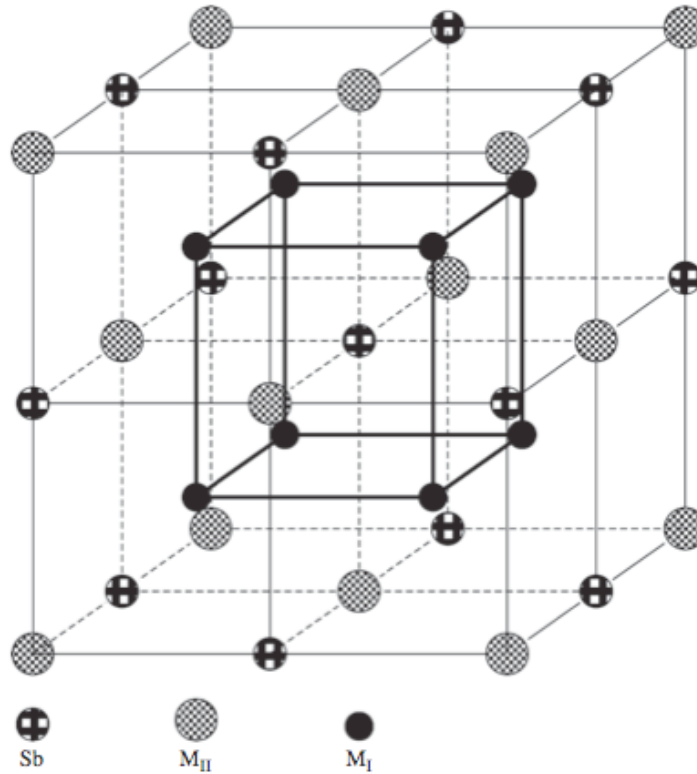
Fig. 3. DO₃ crystal structure.[35]

1.2.2   Positive Electron Affinity (PEA) Semiconductor Cathodes

The three steps model that developed by W. Spicer in 1960s can describe the electrons emission from photocathode. The three steps consist of electron excitation to conducting band, electrons transport and electrons emission to vacuum [36].

Work function of K_2CsSb cathodes is around 1.9eV which allowing them to emit electrons in visible light. In this kind of cathodes, the vacuum level is above the conduction band minimum. The excited electrons need to have energy larger than this vacuum level in order to emit once reach the surface. [32]

1.3   Multi-Alkali Photocathode R&D at BNL

The design of photocathodes for ERL is one of the key challenges. Stony Brook University and BNL work together in several areas including developing of improving cathode fabrication recipe, QE and transverse emittance measurement and test of the cathode in superconducting RF electron-gun. [8, 22, 23]

Storage, transportation and insertion of photocathode in the SRF electron gun are still big challenges. The cathode system includes a preparation chamber and a transportation cart as shown in figure 3. The purpose of this system is to grow robust and high yield multialkali photocathode away from the photoinjector and has a reliable method to transport the photocathode and insert it into SRF gun. This process requires very good vacuum (10 E-11 torr) to maintain its high quantum efficiency during the transportation and insertion into the electron gun. The system designed and produced by Advanced Energy Systems Inc. can meet these requirements. [24]
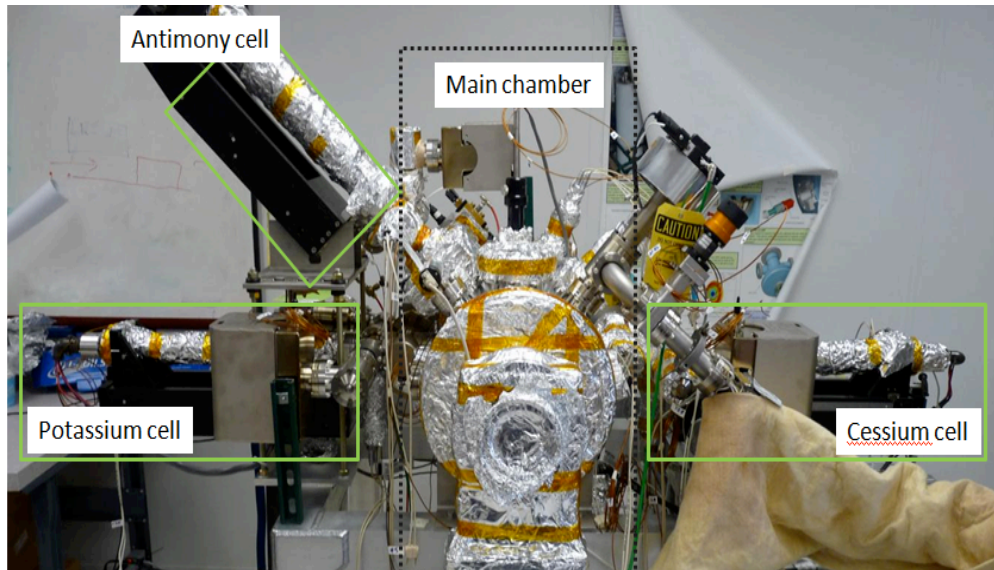
Fig.4 (a)Deposition system at Collider-Accelerator Department(CAD)
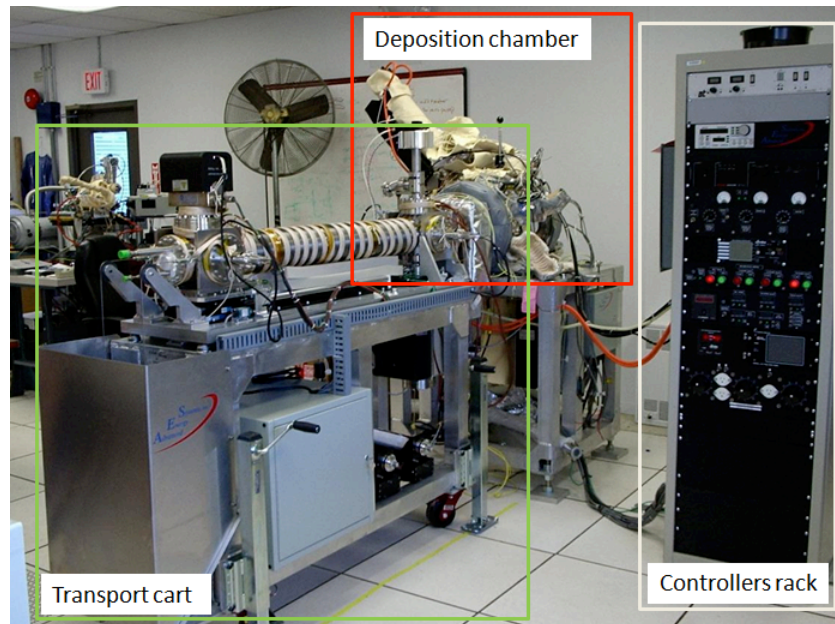
Fig.4 (b) Transport cart attached to depo-achamber for cathode growing and transport to gun

6
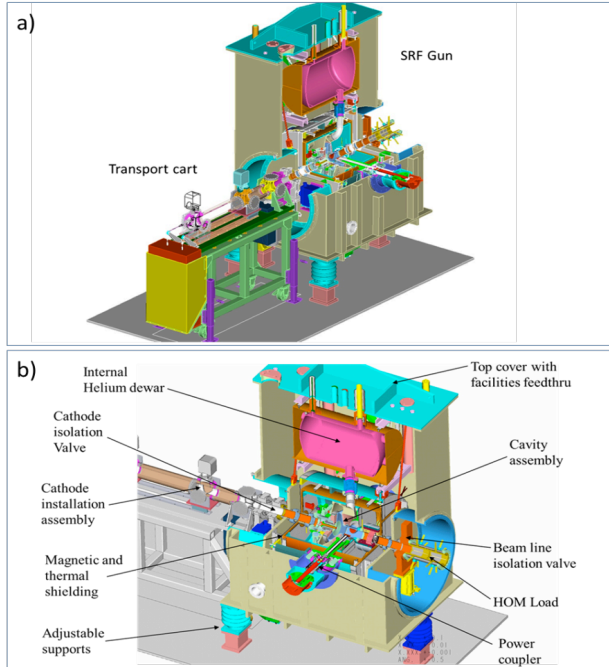
Fig. 5 (a) Overview of the system attachment for cathode transfer. (b) Details of the parts of the equipment.[25]
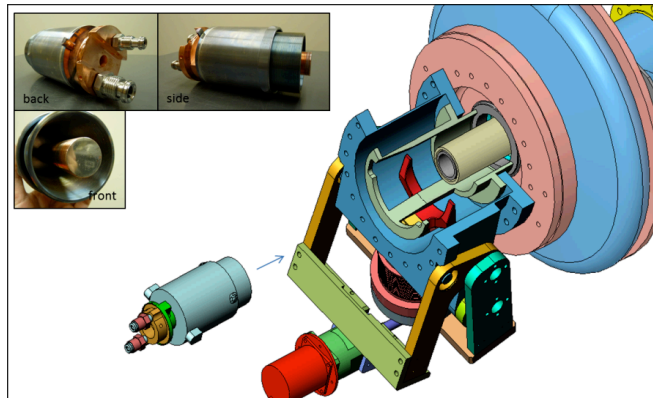
Fig. 6: Top left: Pictures of the cathode stalk. The graphic shows how the insertion of the stalk will take place in the gun.[25]

The collide-Accelerator department at BNL is building a high-average current ERL which is the ERL prototype for the main project for eRHIC——an upgrade of the present RHIC facility. [25-27]

The ERL features a 5-cell 704 MHz SRF accelerating cavity, a highly flexible single-pass loop and a comprehensive system of beam instrumentation. The high QE multi-alkali photocathode is served with a load-lock delivery system. With.[28, 29] Our cathode is deposited on the tip of a stalk. As shown in figure 4, this stalk can be moved from the cathode preparation system to the gun. The cathode stalk is introduced into the gun beam-line vacuum through a pair of gate-valves, one on the transport cart and another one on the gun cathode-side line. Once the

7

stalk moves near its correct position, a special fork can grab the stalk and press it to its final position.[30]

1.4 Motivation

For future user facilities, the focus of our project is on photocathodes for high repetition rate Free Electron Lasers (FELs) and high average current Energy Recovery Linacs (ERLs). The work is concentrated in two areas: 1). Physics and chemistry of alkali-antimonide cathodes; 2) Tests of cathodes in superconducting RF photoguns.

This work will make extensive use of synchrotron radiation materials science techniques, including powder and single crystal diffraction, in plane and out plane reflectivity，X-ray fluorescence, variable energy XPS. The principal requirement is the addition of systems to allow transportation of samples between deposition chambers and the various tools as well as the addition of some tools to deposition systems to obtain key information during cathode growth.

For ERL and FEL applications, there still are many questions remain which need to be considered before we are sure that this can be used in a SRF photo-injectors.

Firstly, growth mode and surface morphology: The growth of the antimonide films is dependent on many parameters: substrate temperature, deposition rate, use of co-deposition, substrate material and structure, etc. Flatness of the surface will be important in determining emittance in a high field gradient, and crystallinity will affect QE as well as the most likely damaging mechanisms.

Furthermore, reliability of manufacture: Reliable recipe of production of K_2CsSb cathodes is still not clear. We need to understand this link between the substrate material and preparation and eventual characteristics of the cathode in much more detail.

Thirdly, the operation in a gun: Operation in a gun environment needs to be evaluated in detail. Ions formed in the residual vacuum can bombard the cathode and cause crystallographic and chemical damage. We need to verify that in the residual vacuum of the gun, we can get good QE and stable thermal emittance over the long periods necessary for an operating facility.

2 Experimental

2.1 Procedure for growing of bi-alkali (K2CsSb) cathode

2.1.1 Deposition system and Instrumentation Requirements
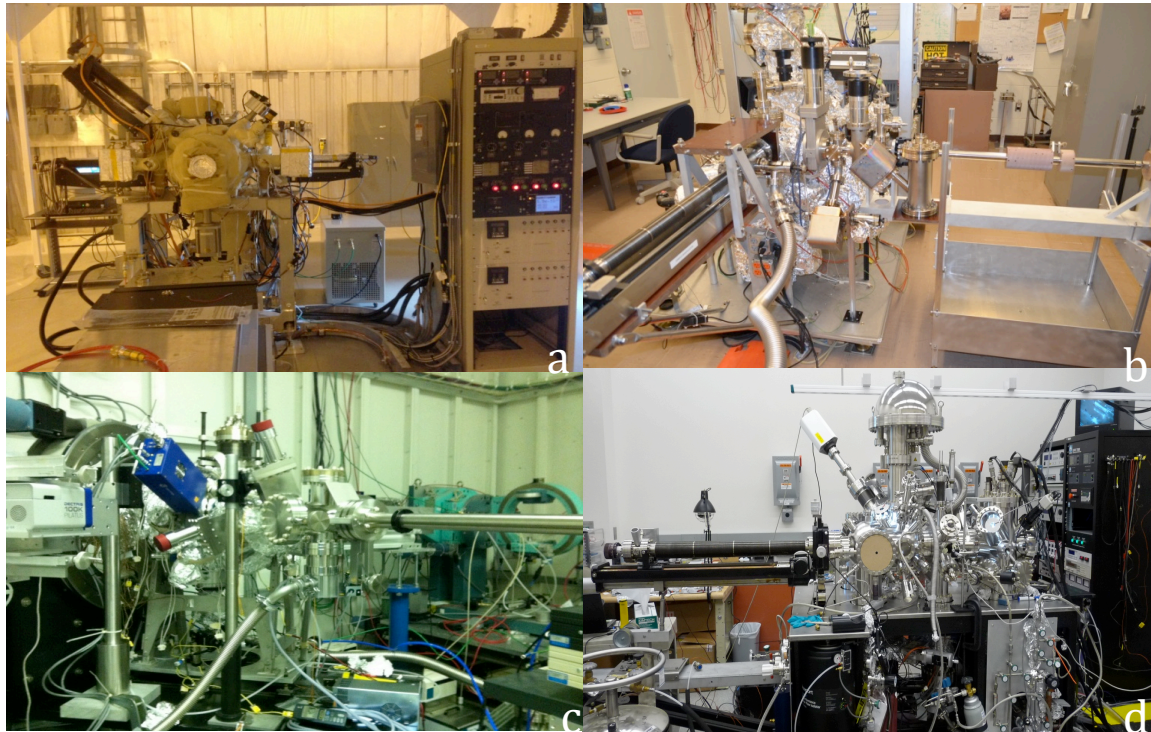
Fig, 7 (a) Deposition and transportation system at Collider-Accelerator Department (CAD); (b) Deposition system at Instrumentation Division; (c) Deposition system National Synchrotron Light Source (NSLS) X21 Beamline. (d) Deposition system at Center for Function Nanomaterials

Instrumentation Requirements:

Film Quartz monitor: INFICON quartz-micro-balance is used to estimate the thickness of the material deposited.

Vacuum Monitoring: Pfeiffer Prisma QMG 200 residual gas measurement is used to records the partial pressures of various residual gases in the chamber

Pressure record: GRANVILLE-PHILLIPS 350/358 Ionization Gauge Controller - Records the total pressure in the prep chamber

Temperature control: Thermocouple+heater are used to control the temperature of substrate.

Power supply: Used to degas and heat the source.

QE measurement system: Laser and photo detector - Used to shine light of known power on the cathode.

Current measurement: KEITHLEY Electrical test instruments system and LabVIEW software.

2.1.2 Procedure

2.1.2.1 Ultra High Vacuum (UHV) achievement

Firstly, the turbo pumps the preparation chamber's vacuum to low10 E-6 torr. Then, bake the entire chamber to 140°C±10°C. 6 thermal couples monitor the temperature of different parts of the whole chamber. At the same time, heat the substrate to around 600 °C to clean the surface of the substrate. After bake 48-72 hours, cool down the system to room temperature. At this moment, the pressure of the chamber should reach low 10 E-11 torr.

2.1.2.2 Cathode growth

Before growing the photocathode, we should verify the deposition chamber is in the UHV regime where low partial pressures of H_2O, CO and CO_2 are achieved. (Usually, there should be no H_2O, CO and CO_2 partial pressure are detected in the RGA). Then check K, Cs and Sb sources are in place and calibrated and ready for deposition. They should be isolated in the arms before assembly of the transport card. This preparation should be performed no more than two days in advance to the assembly of the transport card to the deposition chamber.

The standard procedure is firstly, heating up of the Mo/Cu substrate to ~100 C and then start evaporation of Antimony film. Sb is evaporated from PtSb beads. The goal is to get a thickness of 15 nm.

Once the Antimony film is obtained, the substrate temperature should be increased to ~140 C. Then Potassium deposition starts. At least a thickness of 30 nm should be obtained relying in Film Quartz monitor.

When the Potassium-Antimony film is obtained, the substrate temperature should be decreased to ~130 C. Then Cesium deposition starts. Measurements of the photocurrent created with a green laser will be collected within the anode and this will guide the process. Whenever a peak on this signal is reached the Cs deposition can be stopped.

Once the cathode is ready the arm from the transport card can be retracted so the cathode will be stored in it at UHV.

2.1.2.3 Data collection and QE measurement

Quantum efficiency (QE)

To calculate the QE, we use the following formula:

$$\text{QE} = \frac{R_\lambda}{\lambda} \times \frac{hc}{e} \approx \frac{R_\lambda}{\lambda} \times (1240W \cdot nm/A)\frac{R_\lambda}{\lambda} \times \frac{hc}{e}$$

Where λ is the wavelength of illumination light in nm, h is the Planck constant, e is the elementary charge, and c is the speed of light. QE describe how many electrons we can get from each photon at a given energy and wavelength.

As shown in figure 8, we used LabVIEW to collect our photocurrent when we grow the cathode.
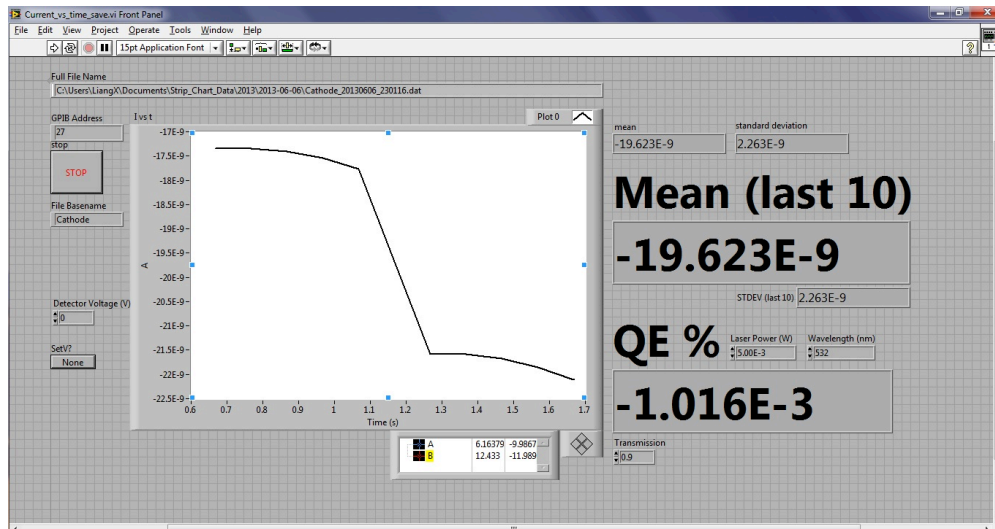
Fig.8 LabVIEW sofeware used to collect the photocurrent

2.2 QE Results analysis and Discussion

2.2.1 The photocathode for 112MHz gun test

2.2.1.1 Cathode substrate selection and preparation

Parallel to the preparation of the SRF gun, important milestones have been accomplished on the way to the test of multi-alkali photocathodes in the 112 MHz SRF gun which is under commissioning. The first step was the selection of the most suitable substrate which could be used into the gun. For this study, several Mulit-alkali photocathodes were grown on Tantalum (Ta), Molybdenum (Mo), and Silicon substrates. And a complete procedure for its characterization was also developed.

Tantalum substrates with different degree of polishing were analyzed. Results for Spectral response on Tantalum substrate are presented in Figure 9. After using the same recipe of growth on both surfaces, small differences in terms of spectral response between polished and unpolished Ta substrates are found. Also QE for both cathodes is similar with a value of 2.53%. These results are valuable information, which allows us to select the more suitable substrates and the level of polishing they are needed for best performance.
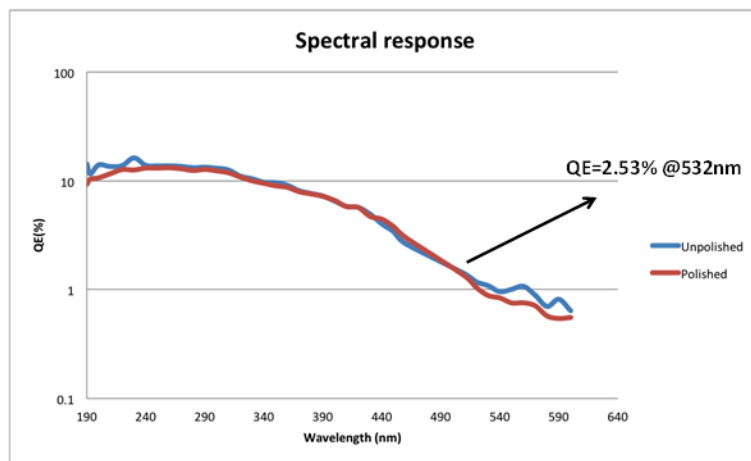
Fig. 9. Spectral response of polished and unpolished Ta substrate photocathode

2.2.1.2 Spatial QE distribution:

Another important aspect that has been studied is the spatial distribution of the evaporation, and how the uniformity of the cathode within millimeter range is achieved after evaporation. This will have important implications in the final performance of the cathode in the gun. The process of growth was similar to the already described and the QE was measured after the evaporation was stopped. Figure 10-a) shows a picture of a Molybdenum sample on which multi-alkali cathode would be fabricated. Figure 10-b) presents the scan through the surface of the cathode. A clear maximum of QE (1.87%) is present in the center of the cathode which confirms the adequate geometry of the experimental set up.
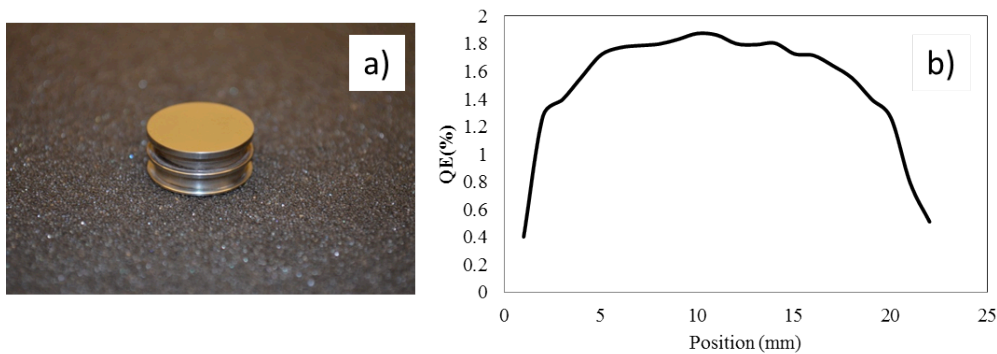
Fig. 10. (a) Polished Moly substrate. (b) QE spatial distribution of the cathode grown across the surface of the Moly substrate

2.2.1.3 QE degradiation in time:

Degradation in time of the cathodes are a big concern and a strong limiting factor when considering the transport of the cathodes from one experimental set up to the other. Many sets of measurements about the decay of lifetime have been performed in order to get a better understanding on the critical parameters. Expected negligible decay within the day scale was found in the case of a cathode grown on Moly substrate, see Figure 11. The excellent UHV conditions during evaporation were maintained once the cathode was prepared and this clearly backups the vacuum conditions of our experimental chambers previous to gun insertion.
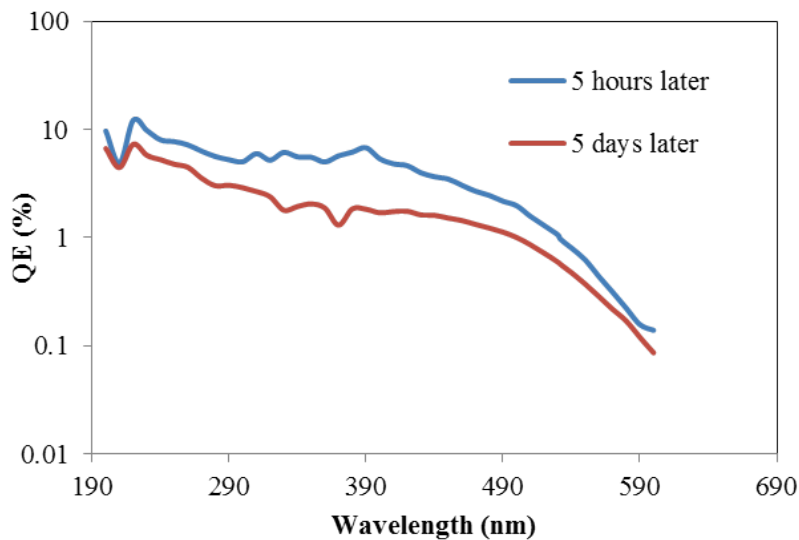
Fig. 11. Spatial QE scan and QE time degradation of Multi-alkali photocathode grown on Mo substrate. Figure shows a QE peak value of 0.96% at 532 nm after 5 hours and after 5 days the QE is 0.56%.

13

2.2.2   Cathode preparation System description

Next tests into the 112 MHz gun cover the use of two K_2CsSb cathodes which will be grown in the deposition system already successfully tested (see Figure 12). This experimental set up reached an important milestone when succeeding in sending two photocathodes to JLab, where they were tested into the HV DC gun and presented a great long lifetime in the order of days.

An important improvement has been performed in Instrumentation Division deposition system that allows connecting a detachable load-lock system including a suitcase and a garage. This has been proved to be a key feature to transport the cathodes efficiently. This way this system provides an excellent flexibility to perform cathodes studies before and after gun insertion.

The plan is that two Molly substrates will sit in the garage, then they'll be transferred into the preparation chamber and K_2CsSb will be grown on top of them. Then, the cathodes will be stored in the garage and moved to the 112MHz gun and be tested. Parameters as current and lifetime will be analyzed.

It is also planned to analyze the crystalline structure of the cathodes before and after insertion into the gun. For this purpose again the flexibility of the garage and load lock will allow to transfer cathodes before and after gun insertion into the experimental set up already available in the NSLS light source (Instrumentation division). It is important to notice that cathode stalk design and fabrication has succeed in produce an standard geometry and dimension of the cathode substrate, so it can be easily transferred between experimental set ups.
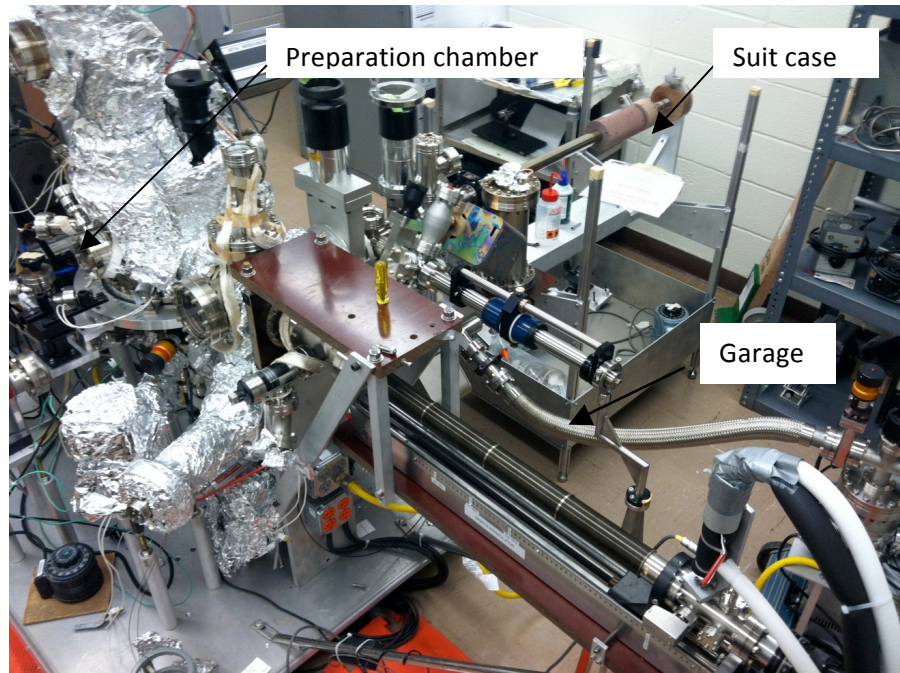
Figure 12 Preparation chamber with load-lock system for 112MHz gun's cathode preparation

3 Structure and Composition Data Analysis

3.1 X-ray Reflectivity (XRR) measurement

X-ray reflectometry measurement (XRR) is a technique through analyzing X-ray reflection intensity curves form grazing incident X-ray beam to precisely evaluate the thickness, roughness, and density of thin films' surfaces. It can work for both single layer and multilayer. [40]

Micro-roughness and the consequent emittance growth with applied field is one important issue which still need us to solve. The theory of relationship between roughness and emittance and the formula are given by D.H.Dowell, and it is proved by T. Vecchione at Lawrence Berkeley National Laboratory. [47]

$$\varepsilon_{rough} = \delta_{x,y} \sqrt{\frac{\pi^2 a^2 E e}{2 m_0 c^2 \lambda_{rough}}}$$

Where a is the amplitude of roughness, λ_{rough} is the characteristic period of the roughness and E is the field gradient

From this formula, we can know that if we want to get low emittince, we need to make sure the roughness of the surface should be low.
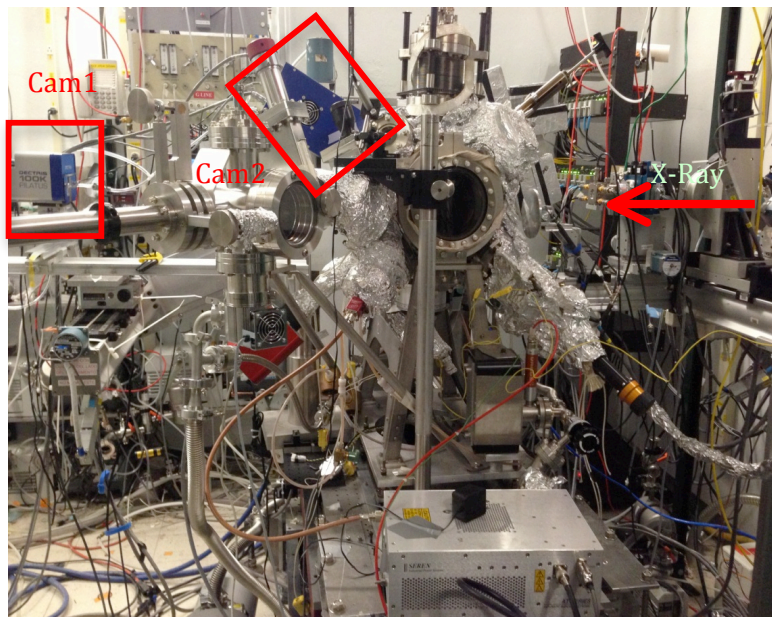
Fig 13 The experimental set up at the G3 beamline at Connell High Energy Synchrotron Source (CHESS) . A 4 axis diffractometer with a UHV chamber allows the in-situ X-ray Reflectivity characterization of cathode growth.

Monochromatic X-rays can generate refracted wave, specularly reflected wave and diffused reflections when they are incident onto the sample surface. If the incident angle on the surface of a substrate is smaller than the critical angel, all incidents X-rays will be reflected. [41,42]X-ray reflectivity decreases rapidly with increasing incident angle above critical angle. X-ray reflectivity is related to the values of refractive index (n) and X-ray wavelength. At NSLS X21 Beamline, the wavelength of the X-ray is 1.2 Å Å(10KeV), and at CHESS G3 Beamline, the wavelength of the X-ray is 1.21 Å (9.8KeV).

The parameters for the experiment:
Distance between sample and camera: 880 mm
pixel size: 0.172 mm X 0.172 mm
camera size: 195 pixel X 487 pixel
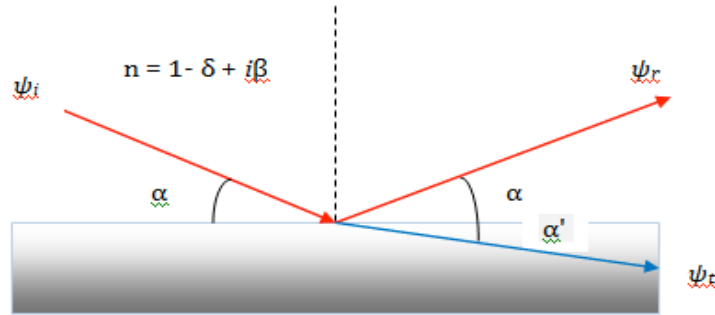
Fig 14. Reflection and Transmission at single Surface

From Figure 14, the reflection and transmission at the single surface, here

$$n = 1 - \delta + i\beta$$

Where δ is the dispersion and β is the absorption. [43]
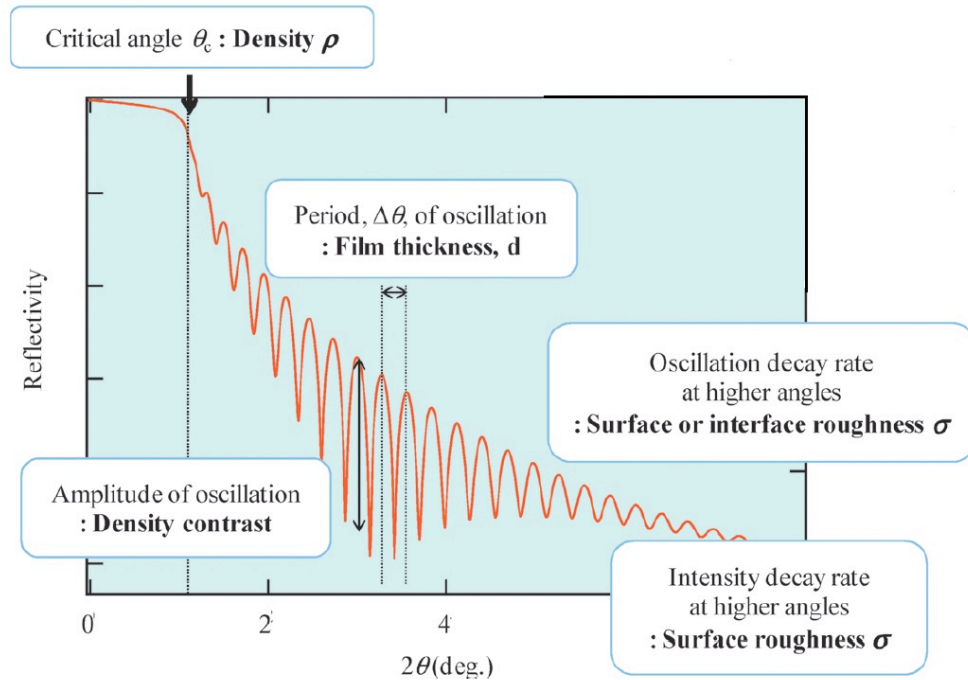
Fig15. Information provided by an X-ray reflectivity measurement [37]

(a). Film thickness

Generally, the Y-axis of X-ray reflectivity curve is shown in a logarithmic scale of the normalized intensity of I/I_0, (a logarithmic scale is used because of the wide dynamic range of X-ray reflectivity intensity)

The reflectivity profile shows oscillations caused by this X-ray interference. (these oscillations were first observed in 1931 by Kiessig and is called Kiessig fringes) the thicker film, the shorter period of the oscillations. [45,46]

Critical angle:

$$1 - \delta = \cos \theta_c \approx 1 - \frac{\theta_c^2}{2}$$

$$\theta_c \approx \sqrt{2\delta}$$

The thickness of the samples is obtained from the period of the oscillations.

$$d = \frac{2\pi}{\Delta q_z} \approx \frac{\lambda}{2\Delta \alpha_i}$$
$$q_z = 2k \sin \alpha_i$$
$$k = \frac{2\pi}{\lambda}$$

(b) . Density

17

The reflection at the surface and interfaces depends on the electron densities difference in the different layers.

The material's density is determined by the critical angle.

For density: we assume that $\beta=0$

$$n_e = \frac{4\pi\theta_c^2}{r_0\lambda^2}$$

where r_0 is the Bohr atomic radius, θ_c is the critical angle and λ is the wavelength of the X-ray.

(c). Roughness
 The larger the roughness of a film would result in the faster the decay rate of X-ray reflectivity.

$r_s\rho$: Scattering length densities

$$\sigma = \exp\left(\frac{-i\pi d\sqrt{n^2 - \cos^2\theta}}{\lambda}\right)$$

Where n is the number of the layer, θ is the incident degree and λ is the wavelength of the X-ray.

Beam alignment

   In this process, the first step is to align the surface of the sample to be paralleled to the direct (incident) beam, and an adjustment of the sample Y axis (dscan chamy -2 2 40 1) so that beam widths are divided into halves by the sample.

1. Set the detector to 0° to detect the direct (incident) beam directly (put filter in to avoide damaging the detector).
2. Set the sample and retract the Y axis to the rear to avoid blocking the direct (incident) beam. And adjust the filter to check intensity in this geometry.
3. Scan and set the Y axis (dscan chamy -2 2 40 1) at which intensity is half the intensity measured in step
4. Scan the sample rotation axis (umv zetamig -2 2 20 1) and adjust the alignment incident X-ray beam to obtain a maximum intensity.
   (umv zetamig CEN , set zetamig 0)
5. Repeat the scans to make sure the beam and the sample surface are properly aligned.

   After the beam alignment, the surface of the sample and the direct (incident) beam are essentially parallel.

The next step for a sample alignment, the direct (incident) beam is adjusted strictly in the total reflection range. The total reflection phenomenon occurs when the incident X-ray beam and the reflected X-ray beam have the same angle with respect to the sample surface.

The total reflection phenomenon is highly sensitive to a change in intensity, which is accompanied by the incident X-ray angle. The angular position of the 2θ axis is set in the total reflection range (0.45° for Si, 0.3°for Sb), and multiple axes are aligned as follows:

To ensure a precise X-ray incidence angle various procedures for an accurate sample alignment are required. To facilitate these complex procedures, the software enabling easy acquisition of an appropriate reflectivity curve has been developed, recently.

Cathode growth:

Two Si substrates were treated in diluted HF solution to etch off the surface oxide layer and rinsed with water. The sample (a) was evaporated Sb at 150 °C and sample (b) was evaporated Sb at room temperature. The base pressure in the growth chamber was low

E-10 Torr. Before deposition, all the sources were degased at a low power. During the deposition, film thicknesses were monitored via a lower quartz crystal microbalance and the photo response current was monitored through Keithelry 6517B electrometer at -100 V bias voltage with the cathode illuminated by a 532nm, 5.6 mW green laser.

	Silicon (a)	Silicon (b)
	Thickness (nm)	Thickness (nm)
Substrate	-	-
Sb Evap	5	5
K Evap	15	16
Sb2 Evap	5	6
K2 Evap	50	53

Tab 1 the thickness of different elements deposited on the Si substrate recored by the QCM

The XRR data was fitted using a MATLAB based simulation codes following Parratt's recursion. By optimizing the fitting curve with the experiment data, film thickness and roughness were obtained and reported in table 1. The mean grain sizes of these Sb films were estimated using the Scherrer equation.

	Silicon (a)		Silicon (b)	
	Thickness (Å)	Roughness (Å)	Thickness (Å)	Roughness (Å)
Substrate	-	4.04±0.67	-	4.84±0.02
Sb Evap	49.76±0.22	1.90±0.12	50.53±0.21	3.37±0.03
K Evap	163.73±0.78	4.83±0.11	110.41±0.41	3.67±0.04
Sb2 Evap	225.08±0.59	4.60±0.09	165.47±0.53	4.11±0.09
K2 Evap	544.18±1.16	7.63±0.06	543.13±2.25	5.17±0.15

Tab 2 XRR result of K-Sb film grown on 150C Si substrate (a) and RT Si Substrate (b)

From table 2, compare first layer K-Sb formation in (a) and (b), the only difference is that Sb in (a) was deposited at 150C and Sb in (b) was deposited at RT. The layer thickness afterSb deposition was almost the same. After K deposition, cathode (a) film thickness was much thicker than (b), this may indicated that K diffused better at 150C than RT. Roughness after Sb deposition, (a) is better than (b), so 150C is a better temperature for Sb film deposition compare with deposited at RT.

3.2   Structure analysis of X-ray Diffraction (XRD)

X-ray diffraction can be used for identifying the atomic and molecular structure of a unknown crystal, by measuring the angles and intensities of specific directions diffracted beams. By using this technique, we can identify the crystalline phase of material, measure the average crystallite size, and determine the ratio of crystalline to amorphous material.

In-situ film growth and X-ray diffraction were performed at the X21 beam line of NSLS at BNL. The incident x-ray beam was 1 mm wide and 0.5 mm high. And approximately 2×10^{12} ph/sec of 10 keV ($\lambda = 0.12$ nm) X-rays were used.
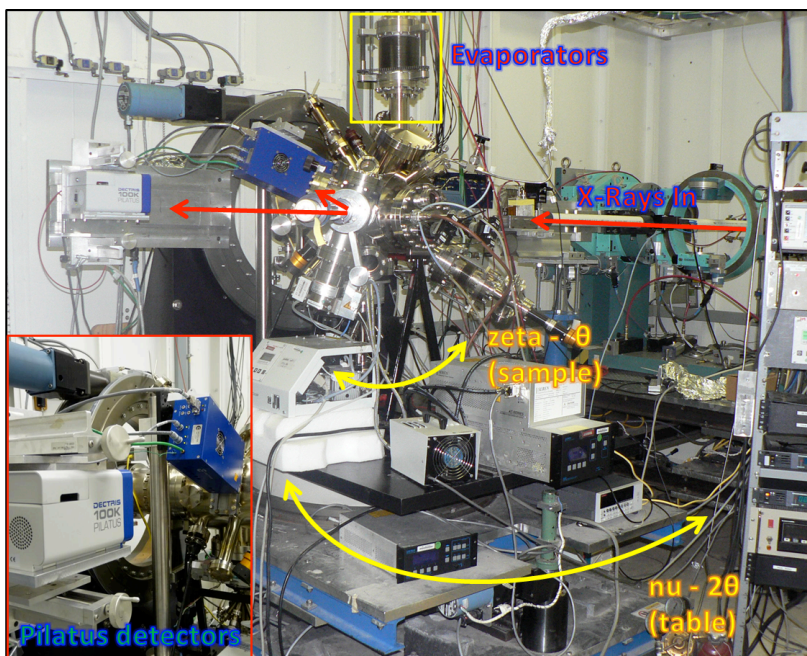
Fig 16. The experimental set up at the X21 beamline at NSLS. A 4 axis diffractometer with a UHV chamber allows the in-situ x-ray diffraction characterization of cathode growth.

From figure 16, we can know the experiment was performed by using a 4 axis diffractometer with two Pilatus 100 K X-ray detectors. One of the detectors was situated in small angle scattering/reflection mode while the other one simultaneously recorded wide angle diffraction data during the deposition.
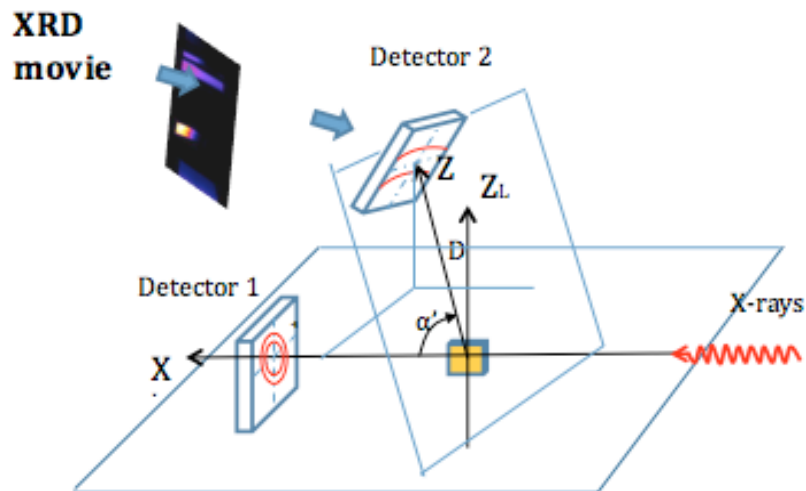
Fig 17. The geometry of the X21 beamline at NSLS.

Figure 17 is the geometry of the X21 beamline. The first detector is at 78.5 cm from the sample normal to the X-ray beam, and the second one is at 19.7 cm with an angle of 25° vertically out of plane. The pressure of the vacuum growth chamber was low 10*E-10 Torr throughout the experiment; an RGA was used to monitored contaminants during growth. Values of H_2O, CO and CO2 partial pressures never exceeded 2x10-10 Torr during deposition, and were typically >5x10^{-11} Torr.

Substrates were electrically isolated during cathode growth. Photocurrent was monitored by applying a negative bias and data was recorded by LabView. Deposition rates were monitored using a quartz crystal film thickness monitor (FTM).

During growth, the X-ray incidence angle was kept at 1.8 degrees onto the substrate, and the nu angle was set to 5 degrees. This resulted in the beam spot overfilling the 2 cm wide sample. After each growth step, out-of-plane scans were taken by rotating nu and zeta.

In-situ XRD has been used to study the growth of each basic element component of the cathode. The substrate was Si (100) which had been treated with HF to remove their native oxide.

Antimony was evaporated from PtSb beads onto the substrate, and the alkalis were evaporated sequentially (potassium then cesium) from Alvatec® sources (S-type). The power supply was used to give some current on the beads and alkalis. When the temperature of the source was going up, they will evaporate Sb, K and Cs to the substrate. For the first sample, this was done with the substrate at room temperature; for the second it was done with the substrate at 100 C. This substrate temperature has previously been shown to affect the crystalline texture of the Sb film.

The substrate temperature was 140 C for K evaporation and 130 C to 135 C for Cs evaporation. The quantum efficiency (@ 532 nm) was monitored during alkali deposition. The

peak QE was 2.7% for the first cathode and 3.7% for the second one. Both cathodes displayed a crystalline structure evolution, with the initial Sb crystal structure disappearing and being replaced by an alkali-antimonide structure.

Figure 18. (a) Left: XRR evolution during K growth. Right: The same procedure was followed camera 2 for tracking the new crystal structure during deposition. For an in-situ deposition Sb film (16.5 nm), the roughness increases very slowly when K-evaporation starts; when evaporate 29nm at 3800s, the fringes are almost the same. At 4645 seconds, the diffused fringes show that K instantaneously reacts and intermixes. As K-evaporation continues, the peak disappears, indicating significant roughness. At this point, the photocurrent reaches the peak, and the QE is 0.1% by using 532 nm laser.   (b) Shows that at the beginning, there is no significant fringes, that mean when we evaporate Sb at 100C , the surface roughness is already very high. After 1180 seconds, the Sb peaks start disappearing. After 2820 seconds, there are some new peaks already appear. At this point, the photocurrent reaches the peak, the QE is 0.4% by using 532 nm laser.
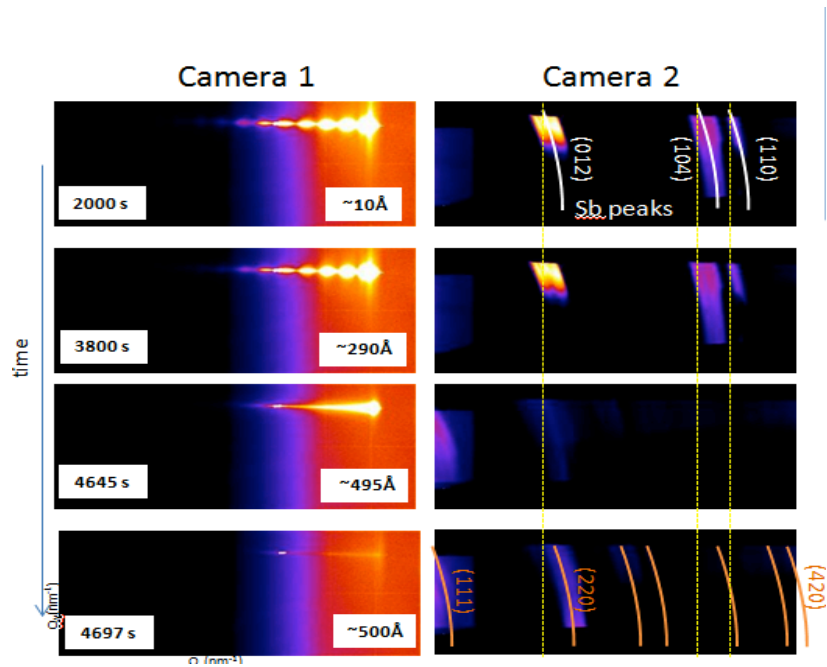
(a)
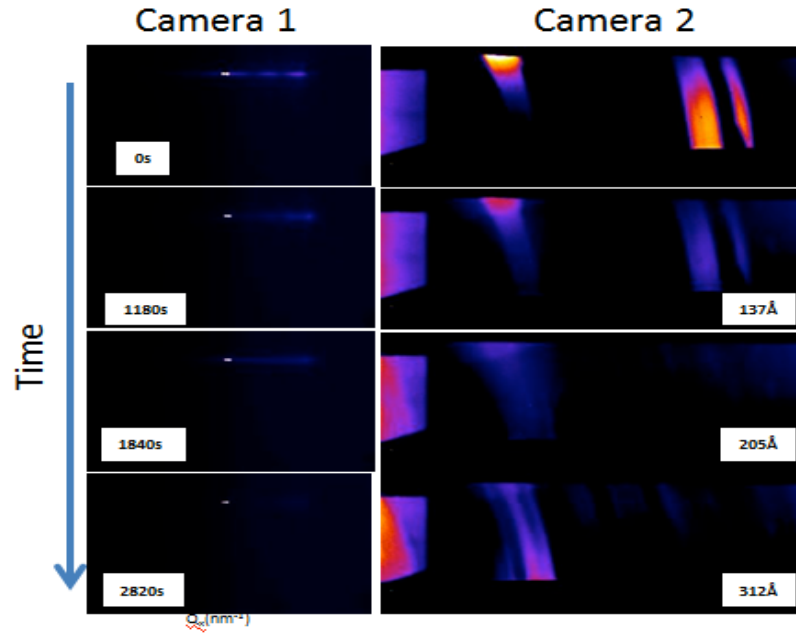
(b)

Fig. 18(a) XRR and XRD evolution during K growth on the Sb evaporate at RT;(b) XRR and XRD evolution during K growth on the Sb evaporate at 100C

Fig. 19. Left: XRR and XRD evolution during K growth on the Sb evaporate at RT; Right: XRR and XRD evolution during K growth on the Sb evaporate at 100C

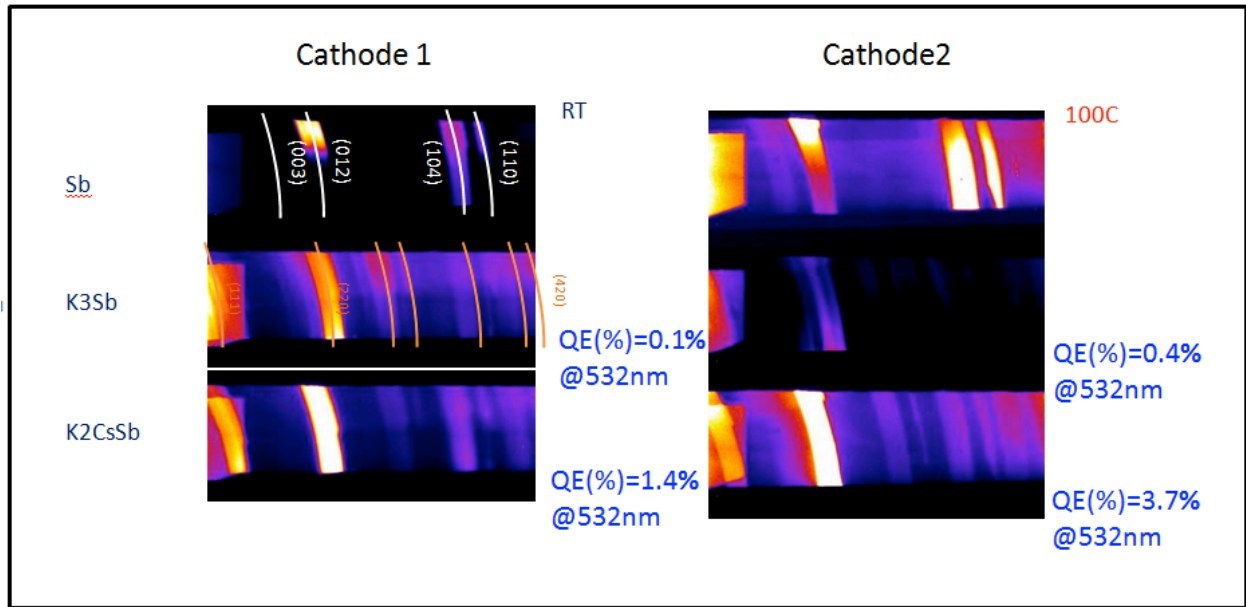From figure 19, comparison between two cathodes grown with different starting points (RT and 100 C Si (100) substrate) has been performed. Differences between these two cathodes suggest that different reaction rates between K and Sb give rise to different final performances of the cathodes. Previous studies have shown that Sb has a very clear [003] surface texture when deposited at RT; the film deposited at 100 C, while still crystalline, lacks this texture. It seems feasible that differences in the original Sb configuration over the Si (100) leads to a different sticking of K, though further analysis of this effect is in progress.

3.3   Chemistry composition analysis by X-ray Photo-electron Spectroscopy(XPS)

X-ray photoelectron spectroscopy (XPS) is a technique used to analyze the surface chemistry of materials.[37] From figure 20 (a), XPS spectra was obtained by irradiating a material with X-rays , and then measure the number of electrons and thekinetic energy which escape from the sample's surface.

Two K_2CsSb photocathodes have been grown in a commercial XPS system (RHK) at the Center for Functional Nanomaterials at BNL. Figure 20 (b) is the experimental set up of this facility. The base pressure of the machine is 0.2 nTorr. Al-Kα X-ray radiation with 1486 eV photon energy was used for the XPS study. From this facility, we can have a deep understanding the interdiffusion process that occurs during growth, as well as observing how the recipe alteration affects the process of growth. This method allows comparison of the final phase of the cathodes grown with different substrates or temperatures, and correlation of these differences with QE. [31]

The cathodes in this experiment were grown on atomically smooth Si [100] substrates. The substrate was not subjected to any ex-situ cleaning to remove the oxide layer on the surface. It was electrically isolated to perform in-situ measurements of the photocurrent produced by a green laser (532 nm).
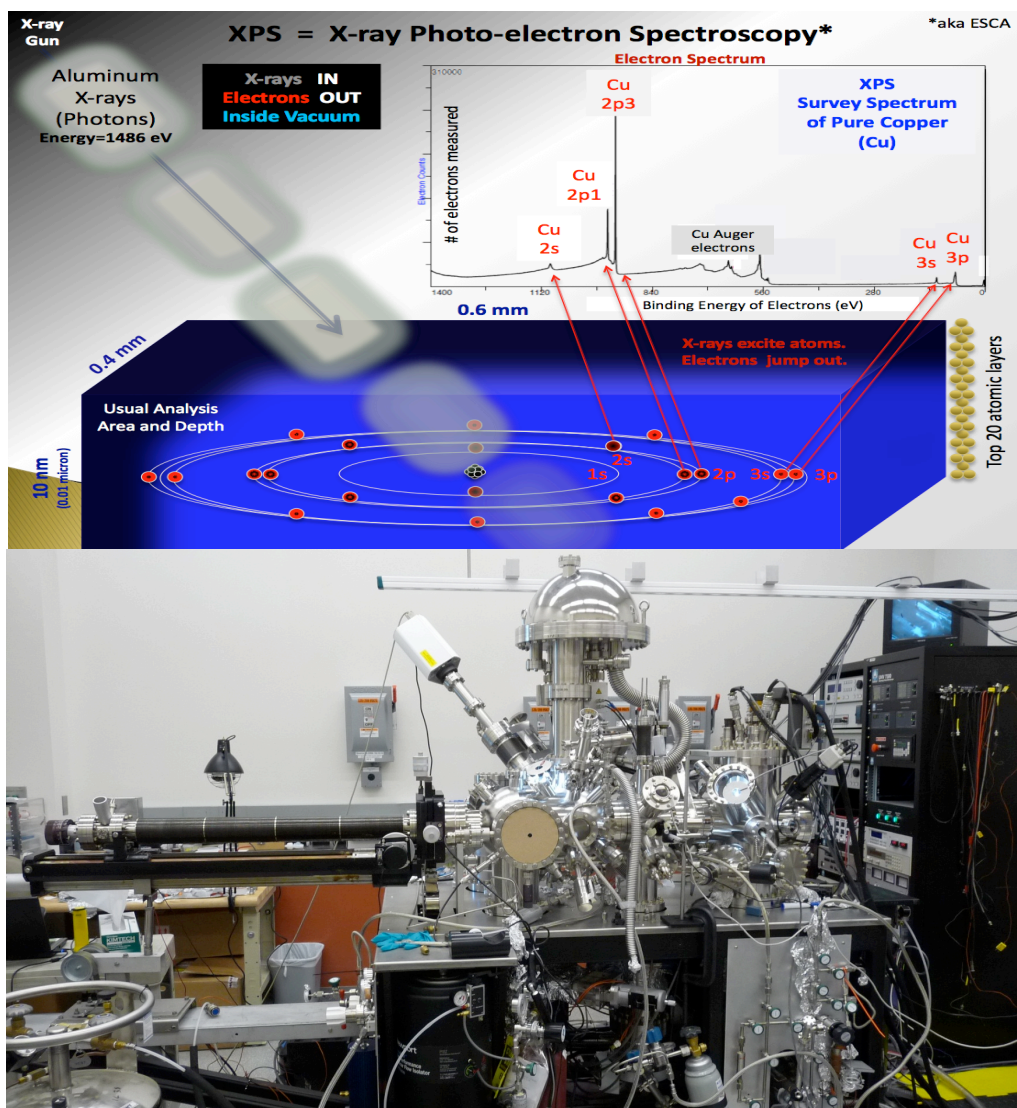
Fig 20 (a) Rough schematic of XPS physics - "Photoelectric Effect. [37](b)The experimental set up at CFN.

For the first cathode, the first layer of Sb was evaporated from PtSb beads, with an estimated final thickness of 24 nm. The $SiO2$ peak is observable from the substrate (Figure 21) initially, but after Sb deposition, it disappears. Suggesting that the Sb layer is thicker than the 5 nm depth, which XPS is sensitive to. For the second cathode, a 10 nm Sb layer was prepared ex-situ within a sputter deposition system, with the sample at room temperature. For this layer, the thickness was checked via x-ray fluorescent analysis in a scanning electron microscope. The Sb film was exposed to atmosphere prior to insertion into the XPS chamber. XPS was used to investigate the oxide formation on the film during this exposure.
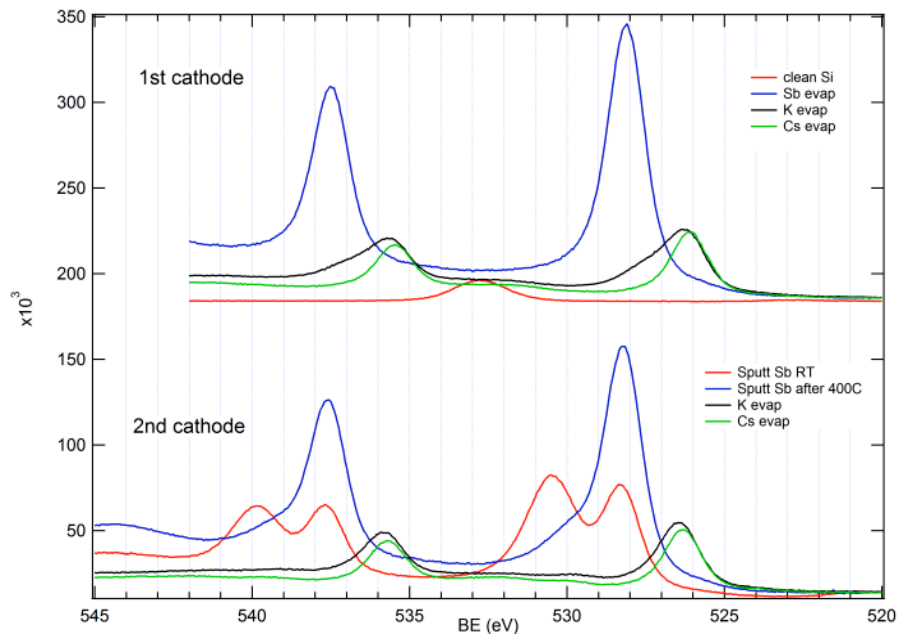
Figure 21 XPS spectra of Sb peaks (3d3/2 and 3d5/2) were obtained before and after each layer deposition. Comparison of both spectra shows small differences; both Sb layers present same strong signal from 3d3/2 and 3d5/2 peaks after the second cathode Sb substrate has been annealed to 400 C, but the shoulder suggests some traces of oxide (Sb2O3 and Sb2O4 or Sb2O5) remain. The Sb signal after K and Cs deposition does not show significant differences among cathodes, suggesting a similar behavior of K and Cs diffusion within the system.

Figure 22 shows the O edge XPS spectra of the film initially, and after heating to 200 C, 400 C and 600 C in vacuum. The original XPS spectrum at RT shows four peaks, suggesting the presence of oxides. The 200 C bake doesn't change this significantly, but the 400 C bake yields a strong Sb signal with much smaller oxide peaks. After 600 C baking, pure Sb signature peaks (3d3/2 and 3d5/2, with energies of 537.5 eV and 528.1, respectively) are lost, suggesting that most of the Sb has formed Sb2O3 (peak at 530.45 eV) and Sb2O4 or Sb2O5 (peak at 539.8 eV). In addition, the substrate SiO2 peak is apparent, suggesting that the Sb film may no longer be contiguous.

Figure 22 Thermal cleaning of Sb sputtered on Si [100] substrate. The substrate was annealed, from room temperature to 600 C, in steps of 200C.

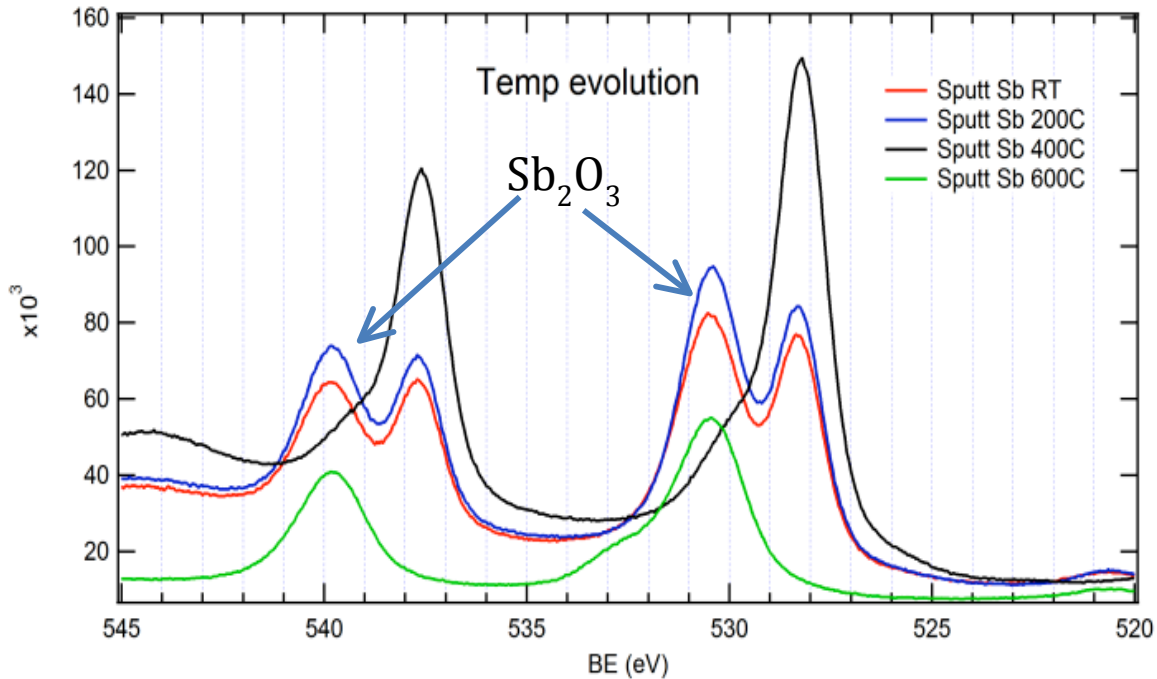For both cathodes, sequential deposition K and Cs was performed while keeping the substrate temperature between 135 and 145 C, this temperature can favor the alkali diffusion between layers. The photocurrent generated from the green laser at 532nm was monitored during deposition; the deposition was stopped when the current reached a plateau. Both substances were evaporated from Alvatec sources, which can produce a very constant and reproducible evaporation rate. K was evaporated before Cs, leading to the formation of a K-Sb compound, such as K3Sb, apart from the pure K on the surface; this phenomenon can be tracked by the decrease of intensity and the shift in both 3d Sb peaks in the black spectral line of Figure 11. Unlike the Sb deposition over Si, the K deposition does not cause a loss of the Sb peaks, suggesting that the K is intermixing with the Sb. No un-reacted Sb is observed within the interrogation depth (5 nm) of XPS.

Cs deposition after K also provokes a small shift and intensity decrease in peaks 3d3/2 and 3d5/2. A slight shift to smaller binding energies and a decrease on intensity is observed. This suggests a stoichiometry change in the Sb which is likely to K2CsSb; an excess of Cs is expected to be on top of the surface layer, balancing between thermal desorption and chemical reaction to adjacent sites. It is well known that the cubic alkali antimonides, K3Sb and Cs3Sb, have a very definite composition and are unstable under alkali excess, so the K2CsSb is the most abundant phase in the final cathode, especially after photocurrent optimization during growth. The final QE in the green was 2.4 % for the first cathode and 0.7 % for the second. Both cathodes were likely too thin for optimum performance at 532 nm, but the first (evaporated Sb) cathode was

more than twice as thick as the second (sputtered Sb). It is also possible that the residual Sb oxide present in the ex-situ sputtered sample even after 400 C anneal may play a role in its reduced performance.

Conclusion:

The evolution of the crystalline structure of multi-alkali cathodes has been investigated via in-situ X-ray diagnostics, including XRD and XRR. The initial Sb layer formation was found to have important implications in the final performance of the cathodes. The final roughness of this initial monolayer of Sb was found to play a key role in the way the subsequent depositions of alkalis (specially the K) diffused and finally crystallized, affecting the final yield. XRD evolution over time revealed complete reaction of K with the Sb at a faster rate when the first Sb layer was grown at 100 C. However, in both cases, all of the Sb was converted to potassium antimonide eventually. Photocurrent measurements during cathode growth allow us to correlate structural crystalline changes with modifications in the yield.

XPS shows that the Sb film rapidly oxidizes when exposed to air; this oxidation can be largely removed by subsequent heating to 400 C. K deposition leads to a shift in the Sb binding energies, with no unreacted Sb near the surface.

4 Future Plan

We still study on the growth mode and surface morphology: The yield of the alkali antimonides seems to be highly related to the growth mode, which in turn is related to the substrate material and crystallinity as well as the precise steps of the deposition process. Even the type of source of Sb, elemental or from de-alloying PtSb, can cause significant changes in initial morphology and subsequent reaction and crystallographic order.

Looking forward, the recipe development is ongoing, and a wider parameter space will be investigated. In the near future, this program will involve testing cathodes in RF photoinjectors and returning them to the diagnostic tools for post-operational analysis. the techniques of x-ray specular reflectivity (XRR) and grazing incidence small angle x-ray scattering (GI-SAXS) to measure the in and out of plane roughness as a function of film thickness. From these techniques, we can demonstrate the growth of Sb, for a range of substrates, temperatures and growth rates, and show the wide range of morphologies that can be formed with relatively minor changes in deposition conditions.

In the ERL side, the ERL project of BNL with a goal of 0.5A average current will be tested. The superconducting RF electron gun operating at 704MHz and 112MHz injectors will be used for testing the brightness and average current of multi-alkali photocathode.

5. Reference

1.   Ben-Zvi, I., Photoinjectors. Accelerator Physics, Technology and Applications, 2004: p. 158-175.
2.   Dowell, D.H., Advances in cathodes for high current RF photoinjectors. Free-Electron Laser Challenges Ii, 1999. 3614: p. 14-21.
3.   Dowell, D.H., et al., Cathode R&D for future light sources. Nuclear Instruments & Methods in Physics Research Section a-Accelerators Spectrometers Detectors and Associated Equipment, 2010. 622(3): p. 685-697.
4.   Bolton, P.R., et al., Photoinjector design for the LCLs. Nuclear Instruments & Methods in Physics Research Section a-Accelerators Spectrometers Detectors and Associated Equipment, 2002. 483(1-2): p. 296-300.
5.   Vecchione, T., et al., A low emittance and high efficiency visible light photocathode for high brightness accelerator-based X-ray light sources. Applied Physics Letters, 2011. 99(3).
6.   Smedley, J., T. Rao, and E.D. Wang, K(2)CsSb Cathode Development. Spin Physics, 2009. 1149: p. 1062-1066.
7.   Rao, T., et al., Photocathodes for the energy recovery linacs. Nuclear Instruments & Methods in Physics Research Section a-Accelerators Spectrometers Detectors and Associated Equipment, 2006. 557(1): p. 124-130.
8.   Srinivasan-Rao, T., et al., Design, construction and status of all niobium superconducting photoinjector at BNL. Proceedings of the 2003 Particle Accelerator Conference, Vols 1-5, 2003: p. 92-94.
9.   Sekutowicz, J., et al., Status of Nb-Pb superconducting RF-gun cavities. 2007 Ieee Particle Accelerator Conference, Vols 1-11, 2007: p. 3161-3163.
10.   Kong, S.H., et al., Cesium Telluride Photocathodes. Journal of Applied Physics, 1995. 77(11): p. 6031-6038.
11.   Burrill, A., et al., Multi-alkali photocathode development at Brookhaven National Lab for application in superconducting photoinjectors. 2005 Ieee Particle Accelerator Conference (Pac), Vols 1-4, 2005: p. 3274-3276.
12.   Todd, A.M.M., et al., Photocathode electron gun applications in research and industry. Application of Accelerators in Research and Industry, 2001. 576: p. 615-618.
13.   Sommer, A.H., A New Alkali Antimonide Photoemitter with High Sensitivity to Visible Light. Applied Physics Letters, 1963. 3(4): p. 62-63.
14.   Dowman, A.A., T.H. Jones, and A.H. Beck, Scanning Electron-Diffraction Studies on Alkali Antimonide Photocathodes, Including S20. Journal of Physics D-Applied Physics, 1975. 8(1): p. 69-84.
15.   Robbie, J.C. and A.H. Beck, Scanning Electron-Diffraction Studies on Cesium Antimonide Photocathodes during Formation. Journal of Physics D-Applied Physics, 1973. 6(11): p. 1381-&.
16.   Dowell, D.H., S.Z. Bethel, and K.D. Friddell, Results from the Average Power Laser Experiment Photocathode Injector Test. Nuclear Instruments & Methods in Physics Research Section a-Accelerators Spectrometers Detectors and Associated Equipment, 1995. 356(2-3): p. 167-176.
17.   Dowell, D.H., et al., The Boeing photocathode accelerator magnetic pulse compression and energy recovery experiment. Nuclear Instruments & Methods in Physics Research Section a-Accelerators Spectrometers Detectors and Associated Equipment, 1996. 375(1-3): p. 108-111.
18.   Dowell, D.H., et al., Results of the Boeing pulse compression and energy recovery. Nuclear Instruments & Methods in Physics Research Section a-Accelerators Spectrometers Detectors and Associated Equipment, 1997. 393(1-3): p. 184-187.
19.   Sommer, A.H., Photoemissive materials: preparation, properties, and uses1968, New York,: Wiley. ix, 256 p.

20.   Sommer, A.H., A new alkali antimonide photoemitter with high sensitivity to visible light. Applied Physics Letters, 1963. 3(4): p. 62-63.

21.   Sommer, A.H., Characteristics of Evaporated Antimony Films as a Function of the Antimony Source. Journal of Applied Physics, 1966. 37(1): p. 174-179.

22.   Burrill, A., et al., BNL superconducting RF guns-technology challenges as ERL sources. Nuclear Instruments & Methods in Physics Research Section a-Accelerators Spectrometers Detectors and Associated Equipment, 2006. 557(1): p. 75-79.

23.   Calaga, R., et al., High current superconducting gun at 703.75 MHz. Physica C-Superconductivity and Its Applications, 2006. 441(1-2): p. 159-172.

24.   D.Pate, R&D ERL-Photocathode Deposition and Transport System. C-AD AP Note.

25.   V.N.Litvinenko, HIGH CURRENT ENERGY RECOVERY LINAC AT BNL. Proceedings of 2004 FEL conference, 2004: p. 570-573.

26.   Pozdeyev, E., DIAGNOSTICS OF BNL ERL. Proceedings of PAC07 New Mexico, USA.

27.   Burrill, A., R&D ERL: SRF Electron Gun. C-AD Note.

28.   Burrill, A., I. Ben-Zvi, et al, BNL superconducting RF guns-technology challenges as ERL sources. Nuclear Instruments & Methods in Physics Research Section a-Accelerators Spectrometers Detectors and Associated Equipment 2006. 557(1): 75-79.

29.   Bluem, H., A. M. M. Todd, et al. , Electron injectors for next generation x-ray sources. Ieee Particle Accelerator Conference, 2007 Vols 1-11: 3797-3799.

30.   Calaga, R., I. Ben-Zvi, et al, High current superconducting gun at 703.75 MHz. Physica C-Superconductivity and Its Applications, 2006. 441(1-2): 159-172.

31.   J.Smedley, IPAC 2011, 2011: p. 3206-3208

32.   http://photocathodes.chess.cornell.edu/wiki/Main_Page

33.   W.; Feinstein , Pantell R.H. SourceA thermionic-cathode RF gun for compact FEL use Authors: Lewellen . Nuclear Instruments and Methods in Physics Research Section A: Accelerators, Spectrometers, Detectors and Associated Equipment, Volume 393, Number 1, 1 July 1997 , pp. 447-450(4)

34.   Sommer A H 1968 Photoemissive Materials (New York: Wiley)

35.   Optical properties of the alkali antimonide semiconductors Cs3Sb, Cs2KSb, CsK2Sb and K3Sb / L. Kalarasse, B. Bennecer , F. Kalarasse/ Journal of Physics and Chemistry of Solids 71 (2010) 314–322

36.   W. E. Spicer A. Herrera-Gomez Modern Theory and Applications of Photocathodes SPIE."s 1993 International Symposium on Optics, Imaging and Instrumentation, San Diego, CA, July 11 -1 6, 1993

37.   http://en.wikipedia.org/wiki/X-ray_photoelectron_spectroscopy

38.   Bvcrist , https://en.wikipedia.org/wiki/File:XPS_PHYSICS.png

39.   Yukinori Kobayashi, ERL-BASED LIGHT SOURCE CHALLENGES, LINAC2012, Tel-Aviv, Israel, 714-718

40.   Miho Yasaka, X-ray reflectivity measurement, The Rigaku Journal, 26(2), 2010

41. Isao Kojima, Boquan Li, Toshiyuki Fujimoto, High resolution thickness and interface roughness characterization in multilayer thin films by grazing incidence X-ray reflectivity. Thin Solid Films 355±356 (1999) 385- 389

42. Hui-Chia Su, Chih-Hao Lee, Ming-Zhe Lin, and Tzu-Wen Huang, A Comparison Between X-ray Reflectivity and Atomic Force Microscopy on the Characterization of a Surface Roughness, CHINESE JOURNAL OF PHYSICS VOL. 50, NO. 2 April 2012

43. Parratt L G 1954 Phys. Rev. 95 359

44. Kenji Sakurai and Atsuo Iida, fourier Analysis of Interference Structure in X-Ray Specular Reflcetion from Thin Films. J. Appl. Phys. Vol. 31 (1992) L 113- L115.

45. S.K> Sinha, Y.P. Feng et al. Off-specular X-ray scattering studies of the morphology of thin films. Physica A231 (1996) 99-110.

46. M. Tolan, X-Ray Scattering from Soft-Matter Thin Films. Springer Tracts in Modern Physics. 148.

47. Dave Dowell, Models of effect of roughness on emittance, Photocathode Physics for Photoinjectors (P3) 2012, Cornell University.

48. T. Vecchione, J. Feng, W. Wan, and H. A. Padmore et al. Effect on Roughness on Emittance of Potassium Cesium Antimonide Photocathodes, IPAC2012, New Orleans, Louisiana, USA